Development and characterization of a novel high entropy alloy strengthened through concurrent spinodal decomposition and precipitation

J. Fiocchi[1,2,*], A. Mostaed[3], M. Coduri[4], A. Tuissi[1], R. Casati[2,**]

1 CNR ICMATE, unit of Lecco, via Previati 1/e, 23900, Lecco, Italy

2 Politecnico di Milano, Department of Mechanical Engineering, via la G. La Masa 1, 20156, Milano, Italy

3 University of Oxford, Department of Materials, Parks Road, Oxford OX1 3PH, UK

4 University of Pavia, Department of Chemistry, University of Pavia, viale Taramelli 16, 27100, Pavia, Italy

Corresponding authors: * jacopo.fiocchi@cnr.it; ** riccardo.casati@polimi.it

Abstract

Strengthening mechanisms, which are commonly exploited by conventional alloys, can be effectively incorporated in high entropy alloys (HEAs) to improve their mechanical behaviour. In this light, compositional modification of equiatomic HEAs can be pursued in order to obtain specific microstructural features. Herein, a face centred cubic CoCuFeMnNi alloy was modified by the addition of a proper amount of Ti; a dedicated thermal treatment allowed to concurrently activate two different phase formation mechanisms, i.e. precipitation and spinodal decomposition. This resulted in a nanostructured microstructure, characterized by the presence of periodic modulations of Cu content and by nanosized coherent $L1_2$ Ni_3Ti precipitates. Such microstructure resulted in a more than 100 % increase of yield strength after ageing treatment and allowed to retain a satisfactory ductility. Advanced microstructural characterization, coupled with the application of semi-empirical models allowed to understand the role of each microstructural feature in determining the alloy's mechanical strength.

Keywords

High entropy alloy; spinodal decomposition; precipitation; CoCuFeMnNiTi; high resolution synchrotron X-ray diffraction; aberration corrected scanning transmission electron microscopy.

1. Introduction

In recent years the search for new metallic alloys has been incredibly boosted by the introduction of the concept of high entropy alloys (HEAs). After the seminal works by Cantor [1] and Yeh [2], the development of such alloys has been initially driven by the search for stable and crystallographically simple solid solutions. Nevertheless, the search for improved mechanical properties led soon enough to the idea of extending the well-known strengthening mechanisms, which are commonly exploited in conventional alloys, to HEAs, too [3]. As a consequence, a mechanistic approach has emerged in the design of new compositions: HEAs are designed from scratch or, more frequently, obtained by modification of pre-existing systems to obtain specific microstructural features. Strictly equiatomic compositions have been abandoned and chemical compositions are finely tailored in order to meet specific goals, such as the activation of twining- or transformation-induced plasticity (TWIP / TRIP [4]), the formation of eutectic structures [5] or to exploit specific strengthening mechanisms [6]. In this regard, strengthening has been pursued through grain refinement [7], plastic deformation [8], precipitation [9], spinodal decomposition [10,11] and formation of interstitial solid solutions [12,13]. The resulting alloys, which are based on multiple elements in considerable amounts and are characterized by complex microstructures, are frequently referred to by the broader complex concentrated alloy (CCAs) definition [14].

Recently, the authors of the present work explored the microstructural evolution of an equiatomic, face centred cubic (FCC) CoCuFeMnNi alloy during dedicated thermal treatments, obtaining a 100 % increase of strength upon ageing [15]. Such improvement of the mechanical resistance was related to the emergence of a maze-like structure, consisting of intercalated, coherent Cu-rich and Cu-poor discs and likely deriving from a spinodal decomposition process.

In this view, it might be of interest to modify the CoCuFeMnNi alloy, so as to induce the formation of suitable precipitates, which might cooperate with the structure resulting from spinodal decomposition in further improving the alloy's mechanical behaviour. Indeed, the formation of nanometric precipitates has been found to be particularly effective and to produce outstanding strengthening in several HEAs based on transition metals: among others, Al-, Ti- and Mo-based precipitates have been frequently pursued [16–18]. Among such dopants, Ti appears to be particularly interesting, as it is a common alloying element in numerous well-known alloys. In particular, Ti, in the presence of Ni, gives rise to the Ni_3Ti phase, whose most stable form assumes an hexagonal crystal structure ($D0_{24}$ strukturbericht, space group $P6_3/mmc$), presenting a stacking sequence intermediate between FCC and HCP [19]. Both marageing steels and Ni-based alloys are commonly strengthened by the presence of Ni_3Ti phase. Heat-resistant Ni-based alloys are frequently characterized, in their service state, by a composite structure composed of a disordered FCC matrix phase (γ) and a coherent cuboidal precipitate with FCC stacking (γ'), which presents an ordered $L1_2$ structure ($Pm\text{-}3m$) and a composition close to Ni_3X, where X can be Al or Ti, depending on the relative availability of alloying

elements [20]. Marageing steels are strengthened by the precipitation of several phases, including among others the Ni_3Ti, which mainly forms within the martensitic (BCC) parent phase [21]. Ni_3Ti, usually called η phase in the context of steels, has been reported to undergo several transformations during different heat treatment stages, moving from the initial formation of Ni,Ti-rich clusters to ordered FCC zones and finally leading to the precipitation of stable particles with hexagonal symmetry [22,23].

As far as HEAs are concerned, the possibility of obtaining Ti-based precipitates has attracted considerable interest in recent years, too. Among others, CoFeNi and CoCrFeNi alloys were modified in several works through the addition of selected amounts of Ti and, frequently, Al, usually in the 4 at.% - 8 at.% range. Such modifications resulted in the formation of a large amount of intermetallic precipitates ascribable to the $Ni_3(Al,Ti)$ composition, with other elements frequently occupying the Ni lattice positions [24]. The obtained precipitates were able to produce an evident increase of mechanical resistance [25], which could sometimes exceed 1 GPa. Concurrently, the presence of ordered precipitates was shown to affect the plastic deformation of the addressed alloys: at high precipitate density the resolved shear stress for twin formation was found to be increased, thus giving rise to a purely shear band - dominated deformation [18,26]. It may be appreciated that, also because of the considerable high amount of Ti added to the selected alloys, the mentioned works report the formation of relatively large ordered nanoprecipitates (up to 50 nm), which may directly interact with dislocations through the shearing mechanism [26,27], whereas the possibility of obtaining extremely fine precipitates, acting through coherency, modulus mismatch and order strengthening, has been addressed to a lesser degree.

In this view, the present work aims at modifying an equiatomic CoCuFeMnNi HEA through the addition of a limited amount of Ti to exploit the superposition of the strengthening effects arising from the Cu-related phase separation and the formation of coherent, possibly extremely fine Ni_3Ti precipitates. A suitable fraction of Ti to be added and a proper heat treatment schedule were designed on the basis of CALPHAD simulations. The alloy's microstructure was investigated by means of multiple analysis techniques, showing that both spinodal decomposition and precipitation did indeed take place. The fairly complex nanostructuring was therefore directly related to the improvement of mechanical properties thanks to the application of dedicated semi-empirical models.

2. Materials and methods

Two alloys, namely the equiatomic CoCuFeMnNi and the modified $CoCuFeMnNiTi_{0.13}$, were produced by vacuum arc remelting (VAR, mod. Leybold LK 6/45) of pure raw materials under low pressure Ar atmosphere. Designed and experimentally verified compositions are reported in Table 1.

Table 1. Designed and measured chemical compositions (at.%) of the CoCuFeMnNi and $CoCuFeMnNiTi_{0.13}$ alloys.

		Co	Cu	Fe	Mn	Ni	Ti
CoCuFeMnNi	**Designed composition**	20.0	20.0	20.0	20.0	20.0	-
	Actual composition	19.7	20.2	19.8	20.1	20.2	-
$CoCuFeMnNiTi_{0.13}$	**Designed composition**	19.5	19.5	19.5	19.5	19.5	2.5
	Actual composition	19.6	19.4	19.5	19.4	19.7	2.4

The obtained buttons were remelted 6 times inside a water-cooled copper crucible to ensure compositional homogeneity. Thereafter, the alloy was cold pressed to improve its workability and finally cold rolled down to 1 mm - thick sheet (80 % cold work). The rolled samples were then solution-treated under Ar atmosphere at 1000 °C for 1 h and quenched in water at ambient temperature (25 °C), to ensure dissolution of second phases and proper recrystallization of the heavily deformed cold worked sheets [28]. Finally, ageing treatments were performed for different durations and at 530 °C, 580 °C and 630 °C. Such temperatures were selected on the basis of the phase stability diagrams calculated by means of Thermocalc (TCHEA4 database) software.

Differential thermal analysis (DTA) was performed on solution-treated samples by a DTA equipment (mod. TA Instruments Q600) in the [100 °C, 1100 °C] temperature range.

Microstructural characterization of samples was performed through different techniques. The crystalline structure of the alloy was investigated by synchrotron-based X-ray diffraction (S-XRD). High resolution Synchrotron Diffraction data were collected at 25°C at the ID22 beamline of the ESRF, in Grenoble, in transmission geometry at incident wavelength λ = 0.3545 Å (about 35 keV). The signal was recorded with a 2D Eiger detector, positioned behind the crystal analysers [29]. The wavelength was calibrated with Si Nist 640 powder reference. The specimens were shaped on purpose in the form of finely polished small bars, about 20 mm long and 1 mm thick in order to fit the sample holder. Reducing the thickness is crucial to minimize sample absorption, still improving random grain orientation. To this purpose, the specimens were rotated during acquisition. The diffraction signal was recorded to get full statistics in the 2θ range between 3° and 50°, corresponding to about 0.9 - 15 $Å^{-1}$ momentum transfer Q.

Metallographic analysis of selected conditions was performed by field emission scanning electron microscope (FE-SEM, Zeiss Gemini) on finely polished and etched (Nital 2% reagent) samples. Samples were prepared for transmission electron microscopy analysis using standard routes as indicated in Ref. [15]. Finally, the structure of the specimens down to atomic scale was investigated by aberration corrected scanning transmission electron microscopy (ac-STEM) using a JEOL ARM-200F operated at 200 keV, equipped with an energy-dispersive x-ray (EDX) spectrometer.

Mechanical properties were evaluated through micro-hardness (Future-Tech FM-810, applying a 300 gf load for 15 s) and tensile tests at room temperature and -70 °C (MTS 2/M, strain rate 0.015 min^{-1}). Tensile samples were obtained from rolled sheets, with their main axis lying parallel to the rolling direction.

3. Alloy design

In the present study, the addition of Ti as alloying element in the CoCuFeMnNi alloy was explored. Therefore, a numerical approach based on CALPHAD method was undertaken to explore the possibility of introducing Ti as a secondary alloying element in the CoCuFeMnNi alloy and verify the actual formation of strengthening phases. Figure 1 a reports the pseudo-binary phase diagram for the (CoCuFeMnNi) - Ti system: it is evident that Ti has a relatively limited solubility in the disordered FCC phase at high temperature (about 5 at.% at 1300 K) and that such solubility steeply decreases at lower temperatures, opening to the possibility of inducing precipitation of reinforcing phases from a supersaturated parent phase. It is also evident that the addition of Ti exceeding 3 at.% would lead to the formation of an increasing amount of intermetallic, likely brittle phases at low temperature, which could degrade the mechanical performance of the designed alloy. In this light, a safety factor of 0.5 at.% was considered and, as a result, an addition of 2.5 at.% Ti was selected for further numerical analysis and experimental investigation. The equilibrium step diagrams for the selected alloy ($CoCuFeMnNiTi_{0.13}$) and its lean counterpart are reported in Figure 1a,b: the evolution of phase fractions in CoCuFeMnNi alloy is quite similar to those reported by previous works [28], although it shows the presence of more phases than in graphs elaborated with older Thermocalc databases [30]. According to the computation results, the alloy microstructure is expected to be dominated by a single disordered FCC phase at relatively high temperature (above 800 °C), whereas a second disordered FCC phase and a BCC one appear at lower temperatures. A second BCC and a tetragonal phase with prototype MnNi crystal structure ($L1_0$ strukturbericht, space group *P*4/*mmm*) are also predicted [31], but these phases have not been observed in any of the experimental works reported in literature. The $CoCuFeMnNiTi_{0.13}$ alloy, in turn, is expected to be characterized by the same two FCC and BCC phases. Besides these phases, the formation of HCP Ni_3Ti phase below 753 °C is predicted. These preliminary simulations confirm that the possibility to exploit the precipitation of secondary phases by decomposition of a parent phase is feasible. The presence of single phase fields at high temperature and the emergence of secondary phases at lower temperature suggests that a thermal treatment based on solution treatment, quenching and ageing could induce satisfactory precipitation hardening. Realistic and desirable candidates for precipitation include the secondary Cu-rich FCC phase, the Fe,Co-rich BCC described by MacDonald et al. [28] and the Ni_3Ti phase.

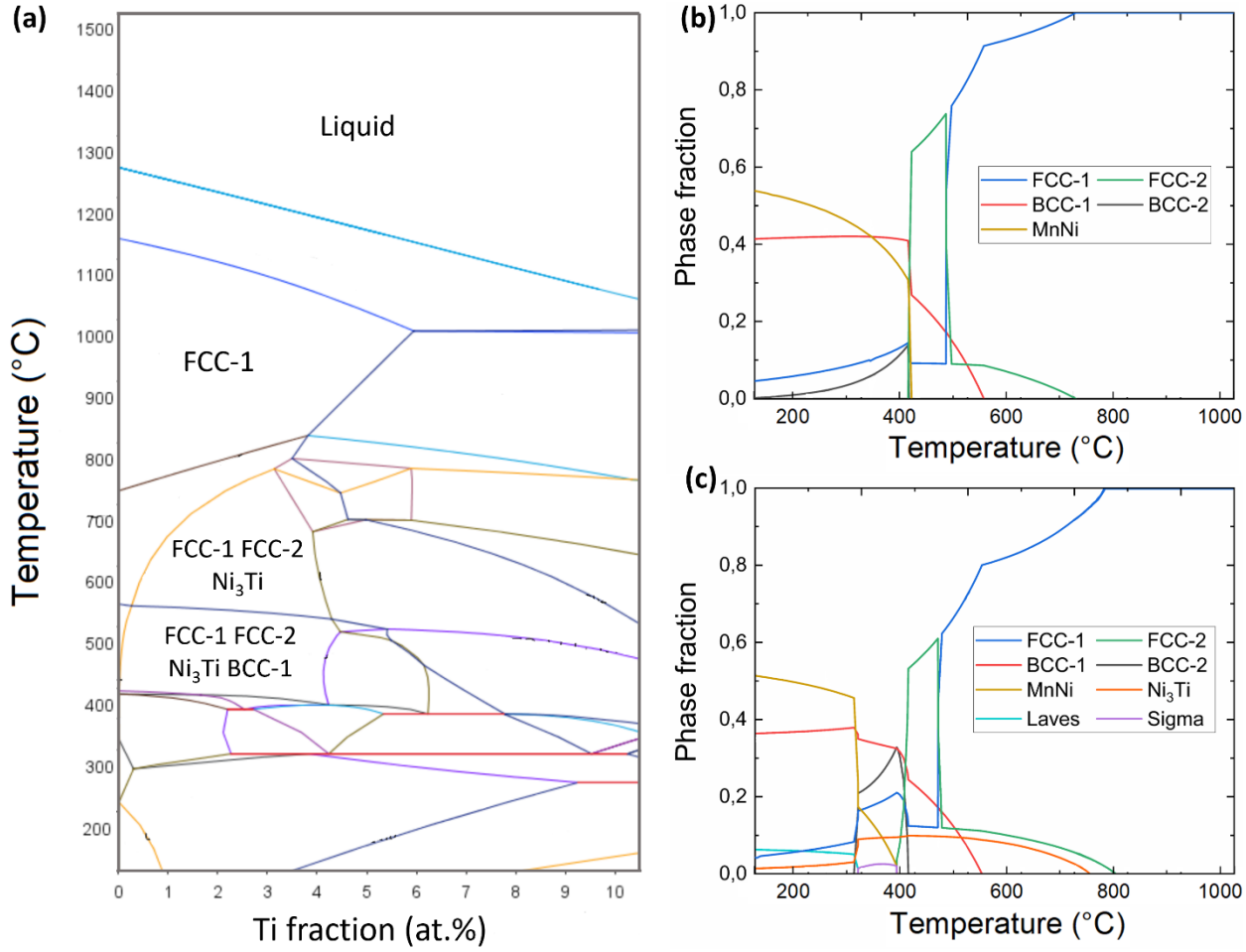

Figure 1. Pseudo-binary phase diagram of the (CoCuFeMnNi) – Ti alloy system (a); equilibrium step diagrams of the CoCuFeMnNi (b) and CoCuFeMnNi$Ti_{0.13}$ (c) alloys.

4. Experimental results

4.1 Definition of a suitable thermal treatment route

DTA and preliminary ageing tests were performed in order to understand whether precipitation hardening could actually take place in the alloys, if subjected to proper thermal treatments. Thermal analysis results (Figure 2) reveal both similarities and differences between the two alloys. As far as CoCuFeMnNi alloy is concerned, a first broad and quite shallow exothermic peak (named as B in the figure) was identified with its maximum lying at 540 °C, whereas two endothermic peaks (C at about 670 °C and D at about 870 °C) were found at higher temperature. According to Sonkusare et al. [30] peaks C and D can be attributed to the dissolution of a Fe,Co-rich BCC phase and a Cu-rich FCC one, respectively, whereas peak B has not been described in previous works. However, it is most likely related to the formation of Cu-rich phases, as suggested by Lin and Tsai for a comparable FeCoNiCr$Cu_{0.5}$ alloy [32]. The Ti-modified alloy presents similar

peak sequence in the higher temperature range (peaks B', C' and D'), which may very well correspond to those identified in the base alloy. On the other hand, an additional exothermic peak (peak A') is located at 360 °C and, conversely, the endothermic peak C' (now lying at 690 °C) appears to be larger than the corresponding peak C. Indeed, the phase stability field predicted by CALPHAD simulation for the Ni_3Ti phase (330 °C – 750 °C) roughly corresponds to the range defined by the exothermic peak A' and the endothermic one C', thus suggesting that these peaks may be related to the precipitation and dissolution of the Ni_3Ti phase. As a further confirmation of the possibility of exploiting precipitation hardening in the alloys at hand, solution-treated samples were aged for 2 h at temperatures in the 380 °C – 780 °C range. As shown in Figure 2 b, hardening took place in both the alloys at all the explored temperatures. It is interesting to notice that the hardness of the Ti-containing alloy shows a strong deviation from the overall trend, namely a 115 HV drop, after treatment at 680 °C. As this temperature closely matches that of the endothermic peak C', this observation further supports the attribution of peaks A' and C' to the precipitation and dissolution of a reinforcing phase, likely the Ni_3Ti foreseen by CALPHAD simulation. Based on these preliminary analyses, the 530 °C – 630 °C temperature range was chosen for further studies, as it appears able to induce maximum hardening for both the base and the Ti-bearing alloys.

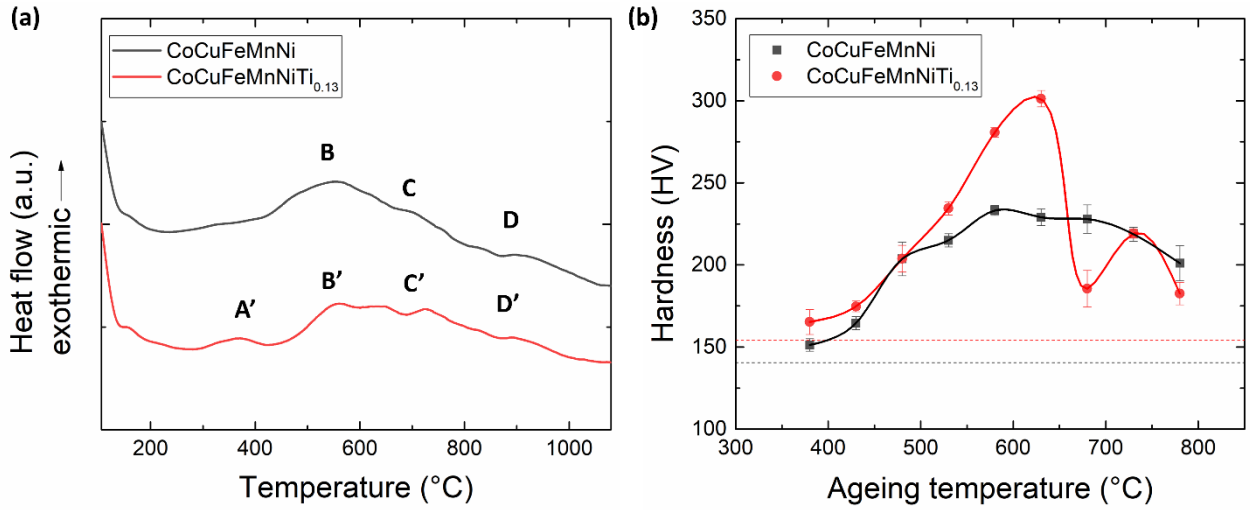

Figure 2. (a) DTA thermogram of CoCuFeMnNi and $CoCuFeMnNiTi_{0.13}$ alloys; (b) hardness evolution as function of ageing temperature of the two alloys (ageing time of 2 hr). Dotted lines indicate the hardness of solution-treated samples.

Thus, isothermal ageing treatments on cold worked and solution-treated samples of both alloys were performed at 530 °C, 580 °C and 630 °C. The hardness values as function of ageing time are collected in Figure 3. The CoCuFeMnNi alloy shows an almost constant behaviour during ageing at 630 °C and 580 °C, both in terms of hardening magnitude and dependency on treatment duration: the trend is characterized by an initial steep hardness increase, from 140.5 HV to 228.8 HV (after 45 min at 630 °C). Thereafter, a much shallower increase up to the maximum (246.2 HV after 6 h at 630 °C) takes place and, finally, this hardening level is

roughly maintained up to 24 h, with no evident indication of overageing in the tested range of time. Only at the lowest temperature (530 °C) some evidence of a two-step hardening process is noticeable, probably related to the formation of the Fe-, Co-rich BCC phase [15,28]. As shown in Figure 3 b, the addition of Ti to the alloy induces a rather different ageing behaviour. Indeed, it can be appreciated that, according to the results reported in Figure 2 b, a more significant hardening is obtained through ageing treatments performed at the three selected temperatures. The maximum hardness increase (from 154.1 HV to 334.5 HV) was reached by aging the solution-treated sample for 6 h at 630 °C. Moreover, the hardening process appears to be much more temperature-dependant, as both the obtained absolute hardening and its response to treatment time change considerably at different temperatures. In particular, the initial hardness increase becomes steeper as the treatment temperature increases and, more importantly, the obtained hardening is much larger with respect to the unmodified alloy. This further confirms that the addition of Ti was able to activate a secondary precipitation process, which is likely based on the Ni_3Ti phase. Again, at all temperatures, no sign of overageing can be detected. Considering these preliminary trials, samples of the two alloys aged at 630 °C for 6 h were selected for further microstructural and mechanical analyses and for comparison with the corresponding solution-treated condition.

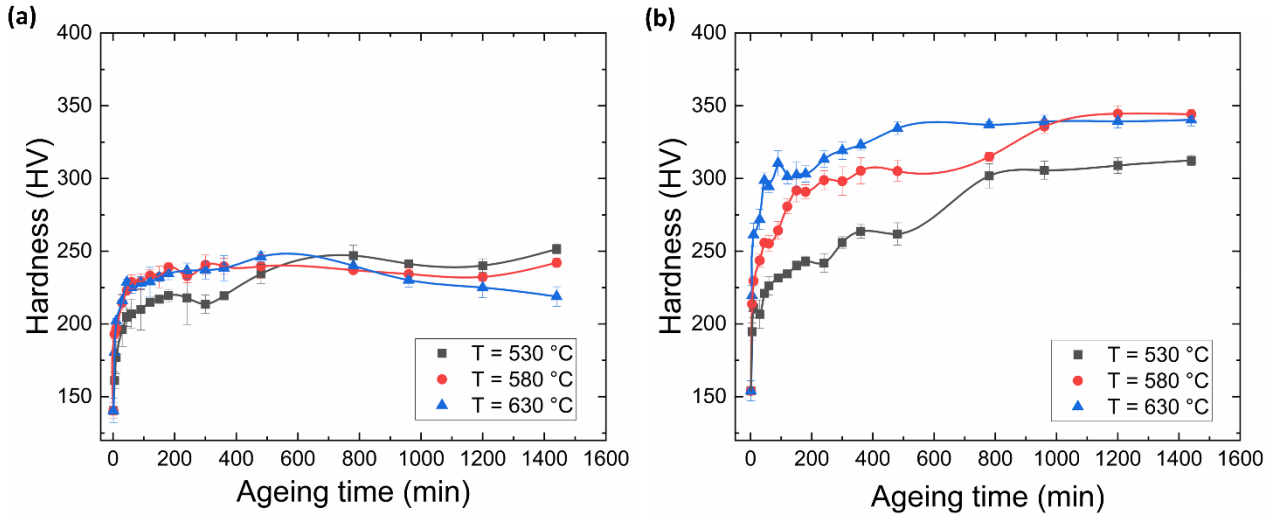

Figure 3. Ageing curves of CoCuFeMnNi (a) and $CoCuFeMnNiTi_{0.13}$ (b) alloys collected on isothermal holding at 530 °C, 580 °C and 630 °C.

4.2 Microstructural evolution

The evolution of microstructure was investigated at multiple scales to understand the nature of phases in solution-treated and peak-aged alloys and their influence on the mechanical behaviour. The observed microstructures were compared to those of the CoCuFeMnNi alloy, which were described in a previous work

by the authors: the reader is kindly asked to refer to ref. [15] for direct comparison of microstructural features of CoCuFeMnNi and $CoCuFeMnNiTi_{0.13}$ alloys. Figures 4 and 5 show the results of the FE-SEM, S-XRD and ac-STEM analyses.

The microstructure of the solution-treated $CoCuFeMnNiTi_{0.13}$ alloy consists of equiaxed grains (20.2 µm on average in size, see Figure S1 in supporting material), featuring faint contrast variations in their interior (Figure 4a). Such structures were also observed by ac-STEM (Figure 4c,d). In particular, the bright globular areas, featuring a size of approximately 10 nm, exhibit coherent interfaces with respect to the surrounding matrix and are indeed defined by their composition. As shown in Figure 4 e, the particles are characterised by an evident Cu enrichment and depletion in Fe and Co, giving rise to a periodic modulation of the local composition throughout the matrix. A much lower variation of the local amount of Ti was also detected. XRD analysis shows that the alloy consists of a single FCC phase, *Fm*-3*m*, characterized by a cell parameter a = 3.62394(1) Å. A Le Bail fit is shown in Fig 2a. No evidence of peak splitting (see highlight on 200 reflection) nor superstructure peaks is observed. Such a result confirms that, similarly to the CoCuFeMnNi alloy, the local compositional variations do not affect the long range ordering.

The ageing treatment at 630 °C after solution annealing induced the appearance of a maze-like structure in the interior of grains and some elongated second phases lying along grain boundaries. The ac-STEM results displayed in Figure 5 reveal that the maze-like structure is composed of intercalated, coherent, Cu-rich and Cu-poor layers. Indeed, Cu-rich areas take the shape of ∼15 nm-thick, mutually orthogonal discs lying on the $\{100\}_{FCC}$ planes of the matrix. The grain-boundary phase is also rich in Cu and coherent to the matrix. A limited amount of Ti was found to segregate along grain boundaries. S-XRD (Figure 5b) reveals the formation of new satellite peaks around those of the FCC matrix phase, which has lattice parameter 3.617(X)Å and sharp signals. The high angle signals show that any original FCC peak has more contributions. The full pattern was modelled considering more disordered FCC phases (*Fm*-3*m*), with different lattice parameter, spanning from 3.596 to 3.633 Å, likely reflecting different chemical compositions. An example of Le Bail fit of the first five reflections is shown in Fig. 5 b, with the 200 reflection magnified in the panel. The satellite peaks (consistent with lattice parameters 3.633 and 3.606 Å) are broader than that of the matrix, likely suggesting a limited domain coherence, consistent with the AR-STEM analysis. Thus, the pattern is consistent with the formation of secondary phases having the same structure of the matrix, but different chemical composition, which reflects on a different lattice parameter.

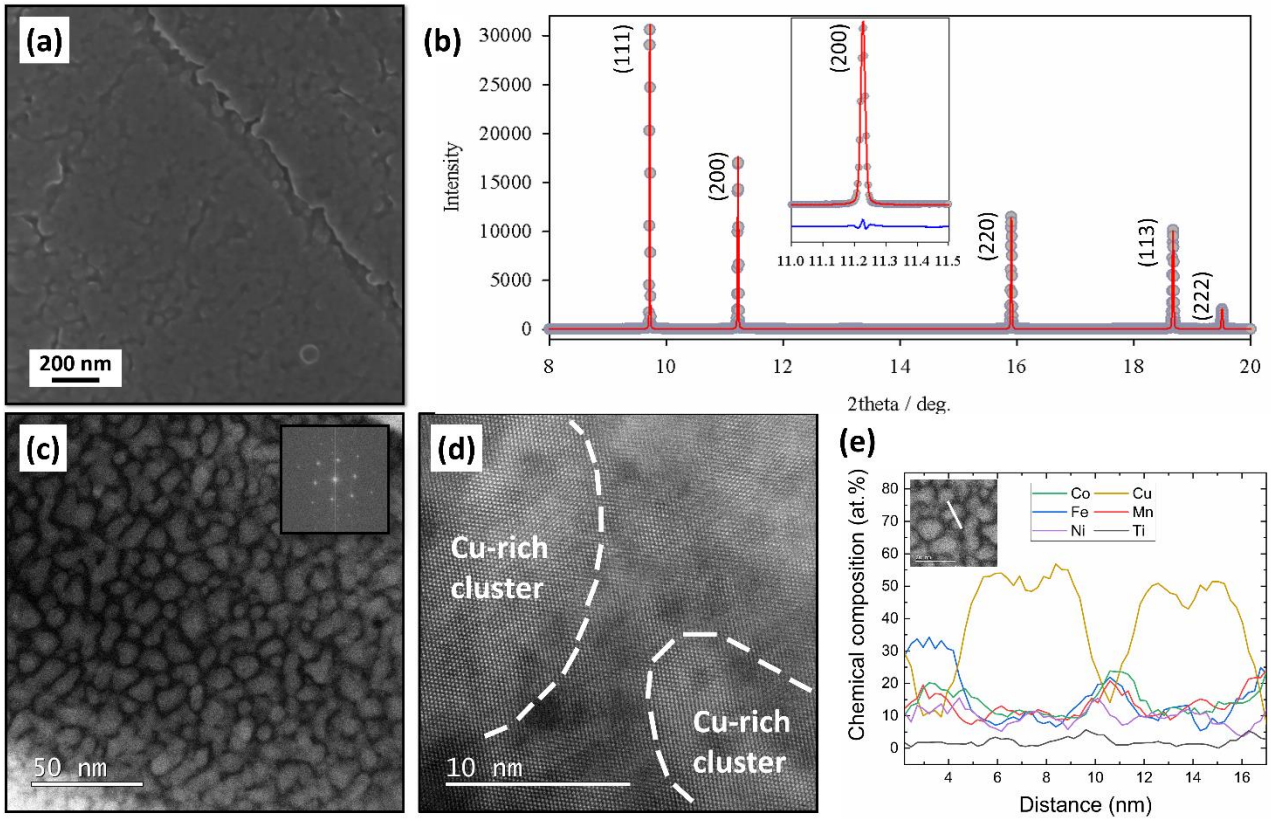

Figure 4. Results of microstructural characterization of the $CoCuFeMnNiTi_{0.13}$ alloy solution-treated at 1000 °C for 1 h: (a) FE-SEM micrograph, (b) S-XRD pattern with a magnification of (200) reflection, (c) and (d) anular dark field (ADF-) STEM images with a viewing direction close to [110], (e) EDX line scan obtained across the matrix.

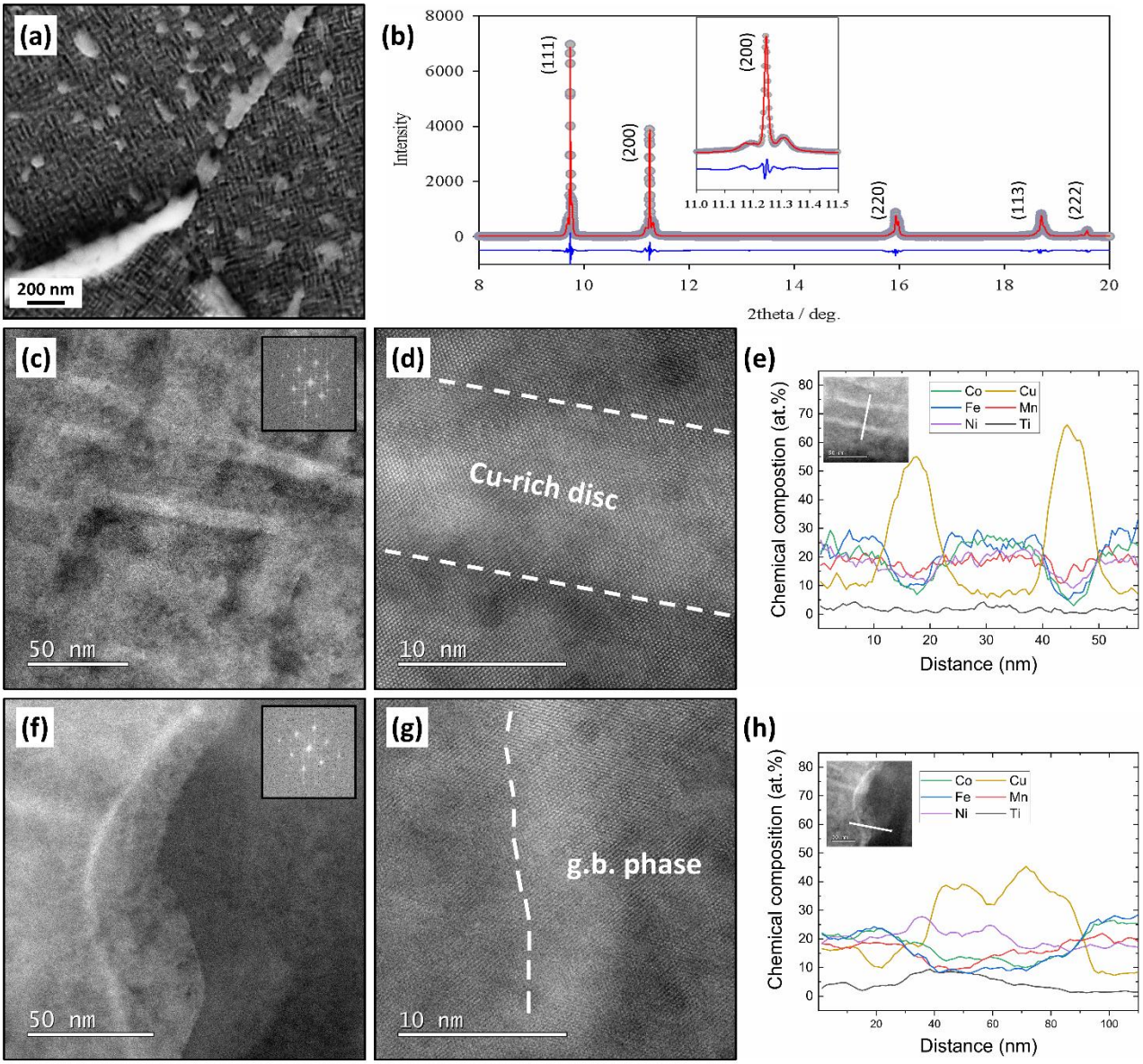

Figure 5. Results of microstructural characterization of the $CoCuFeMnNiTi_{0.13}$ alloy, aged at 630 °C for 6 h: (a) FE-SEM micrograph, (b) S-XRD pattern with a magnification of (200) reflection; (c) and (d) ADF-STEM images of the maze-like structure obtained close to [110] zone axis, (e) EDX line scan obtained across the matrix; (f) and (g) ADF-STEM images acquired from a grain, (h) EDX line scan obtained across the grain boundary shown in (g).

A deeper study of ADF-STEM results, based on the analysis of Fast Fourier Transform (FFT) patterns extracted from the obtained images, was conducted. Figure 6 reports a magnified micrograph of the $CoCuFeMnNiTi_{0.13}$ alloy in peak-aged condition and the related FFT pattern. In fact, Figure 6 a shows some fine rounded areas, about 3 nm in diameter, characterized by different contrast and the FFT pattern presents a relatively complex overlay of different patterns. Besides the larger spots, which are related to the previously described FCC

phases (yellow circles, zone axis close to [110] direction), a second set of spots emerges (red circles). Such spots belong to an ordered phase based on the same FCC stacking observed along [112] zone axis. This second set of reflections features a distance between adjacent spots which is $\frac{1}{2}$ of the spacing characterizing the matrix, thus suggesting that a reduction in symmetry and an expansion of the unit cell took place with respect to the matrix [33]: the matrix displays an average unit cell parameter of 3.55 Å (close to the value measured by S-XRD), while the second set of fainter reflections refers to a unit cell of 7.07 Å., with a reduced lattice parameter close to that of the matrix. These features lead to the conclusion that the red-circled spots are superlattice reflections, belonging to an $L1_2$ structure [25,34–36], i.e. consistent with the ordering of the original FCC cell leading to *Pm*-3*m* space group. Apparently, such superlattice presents a definite orientation relationship with the matrix, as $\{\bar{1}1\bar{1}\}_{superlattice}$ planes are parallel to $\{\bar{1}\bar{1}1\}_{matrix}$ planes. Evidence of superstructure reflections were not revealed from S-XRD. This is likely due to the low relative intensities of superstructure peaks, which become problematic to resolve from the background when characteristic of secondary phases. In addition, the growth of low symmetry domains leads often to the formation of antiphase boundaries with consequent broadening of superstructure peaks, which become more arduous to resolve from background [37,38].

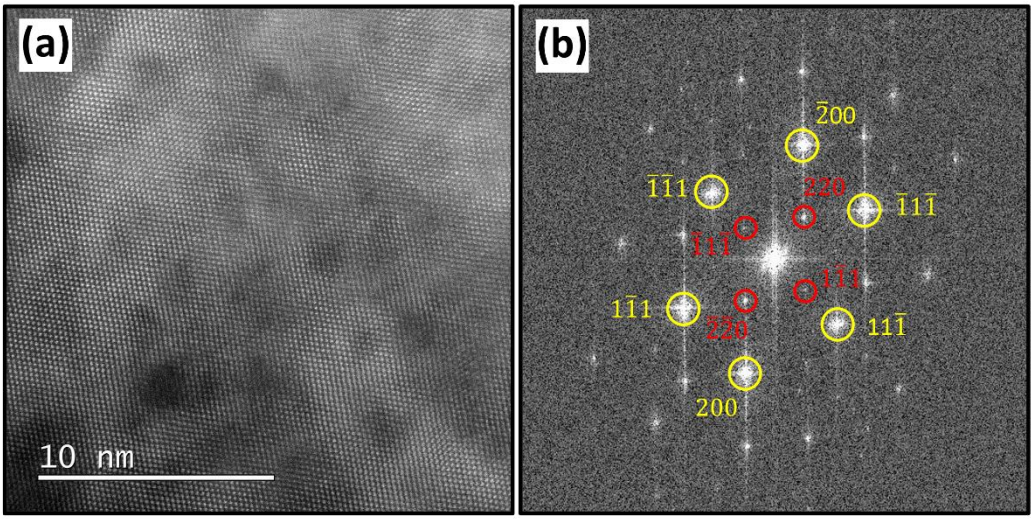

Figure 6. ADF-STEM image obtained close to [110] zone axis (a) and related FFT pattern (b) of the $CoCuFeMnNiTi_{0.13}$ alloy peak-aged at 630 °C.

4.3 Mechanical properties

The influence of microstructural evolution on the mechanical behaviour of the considered alloys was explored through tensile tests at both ambient temperature (25 °C) and at – 70 °C: in particular, solution-treated and peak-aged samples were considered. An overview of the stress – strain curves obtained at ambient and cryogenic temperatures is depicted in Figure 7 a and b, respectively. The corresponding yield strength (YS), ultimate tensile strength (UTS) and elongation to failure (ε) values are reported in Table 2. It

may be immediately appreciated that, coherently with the results of hardness tests, the addition of Ti induced a significant increment of mechanical resistance in both the solution-treated (+ 29 %) and peak-aged (+ 47 %) conditions, also confirming that ageing is more effective in the Ti-bearing alloy. Conversely, no reduction of ductility was induced by the presence of Ti. At -70 °C, the lean CoCuFeMnNi alloy shows an improvement of both strength and ductility. Conversely, the Ti-modified alloy shows an improvement of low temperature strength in the peak-aged condition, whereas no such increment is visible for the solution-treated alloy. As expected, the failure of all tested samples took place in a ductile mode and the resulting fracture surfaces (see Figure S3) appeared to be decorated by a high number of relatively small dimples: coherently with the measured ε values, solution treated samples displayed the largest dimples. Moreover, it may be underlined out that no sign of cleavage or intergranular fracture could be observed, not even in peak-aged samples: this point confirms that the formation of Cu-rich grain boundary phase does not lead to a weakening of the grain boundaries themselves.

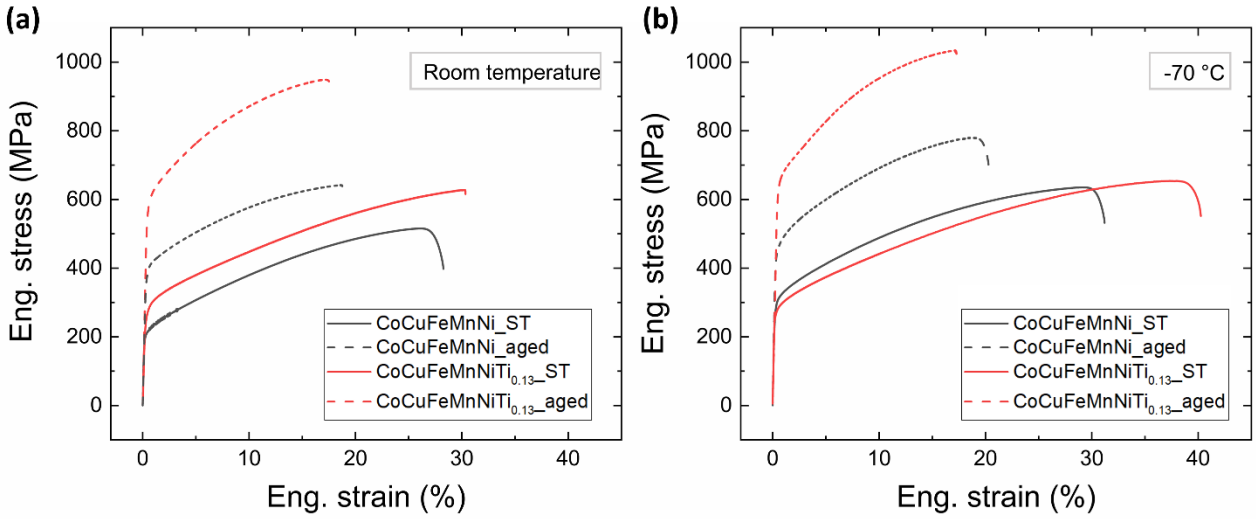

Figure 7. Engineering stress-strain curve of the CoCuFeMnNi and CoCuFeMnNi$Ti_{0.13}$ alloys in the solution-treated and peak-aged (630 °C) conditions tested at room temperature (a) and at – 70 °C (b).

Table 2: Average yield strength, ultimate tensile strength and elongation to failure values of CoCuFeMnNi and CoCuFeMnNi$Ti_{0.13}$ alloys in solution-treated and peak-aged conditions, tested at room temperature and at – 70 °C

		CoCuFeMnNi		**CoCuFeMnNi$Ti_{0.13}$**	
		Solution-treated	Peak aged	Solution-treated	Peak aged
25 °C	YS (MPa)	208 ± 4	398 ± 7	269 ± 3	585 ± 6
	UTS (MPa)	516 ± 9	642 ± 5	628 ± 8	949 ± 12
	ε (%)	28.3 ± 0.1	18.5 ± 0.3	30.4 ± 0.3	17.7 ± 0.2
-70 °C	YS (MPa)	300 ± 10	449 ± 12	271 ± 9	644 ± 8

UTS (MPa)	635 ± 15	771 ± 17	666 ± 10	1032 ± 3
ε (%)	31.2 ± 0.2	20.3 ± 0.3	40.7 ± 3.0	17.3 ± 0.1

5. Discussion

5.1 Phases formation mechanisms

As discussed in a previous paper [15], the process giving rise to Cu-rich clusters in the solution-treated condition and to Cu-rich maze like structure after ageing bears several distinctive characteristics typical of the spinodal decomposition, including the formation of periodic compositional fluctuations, same crystal structure of the resulting phases and coherent interfaces. In this respect, it is well known that the Cu-Fe and the Co-Cu-Fe phase diagrams, contain a submerged miscibility gap [39,40]. Inside such miscibility gap two areas can be distinguished: a first one where phase separation takes place by nucleation and growth, and a second one, where the solid solution becomes unstable against local compositional fluctuations, thus leading to spinodal decomposition [41]. Therefore, such miscibility gap is likely to trigger the decomposition of the supersaturated solid solution by either precipitation or spinodal processes. In particular, copper precipitation has been reported in several steels and HEAs [42], whereas spinodal decomposition through local compositional fluctuations and short-range diffusion was shown to take place in concentrated FCC Fe – 50 % Cu alloys obtained by mechanical alloying [43,44]. It should also be underlined that the decomposition process could not be suppressed by the rapid quenching from solution treatment temperature, as would be expected for a precipitation process. Finally, spinodal decomposition has also been frequently shown to be an exothermic phaenomenon [45] and to be generally related to broad and shallow DSC/DTA peaks [46], similar to those described in Section 4.1: considering the above-reported discussion, it is now possible to attribute DTA peaks B and B' in Figure 2 to the process giving rise to Cu-rich disc-shaped phases in both alloys.

The addition of Ti did not significantly alter the decomposition process or the resulting Cu-rich phases. The most notable effect was a limited segregation of Ti along the interfaces of the Cu-rich clusters in the solution-treated alloy and at the borders of the Cu-rich grain boundary phase in peak-aged samples. Moreover, an increase in the lattice parameter from 3.616 Å (CoCuFeMnNi) to 3.624 Å ($CoCuFeMnNiTi_{0.13}$) was noted in solution-treated samples. This suggests that dissolved Ti, having a larger atomic radius than all other alloying elements, does expand the unit cell volume. On the other hand, the ageing treatment would be expected to induce the precipitation of some Ti-containing phase, as intended in the alloy design phase and as predicted by CALPHAD simulations. Indeed, the formation of HCP Ni_3Ti precipitates was numerically predicted but no sign of such phase could be observed through microstructural analyses. However, the superlattice spots in the FFT analysis of peak-aged $CoCuFeMnNiTi_{0.13}$ alloy correspond to those expected in case of precipitation

of an ordered cubic form with FCC stacking, consistent with $L1_2$ strukturbericht type. The fact that these precipitates are observed only after addition of Ti points towards the formation of $L1_2$ Ni_3Ti. Unfortunately, it was not possible to precisely distinguish the areas characterized by such crystal structure: it may be possible that some of the darker spots visible in Figure 6 are indeed Ni_3Ti clusters. Although their composition cannot be totally confirmed, as their dimension lies below the resolution threshold of the employed EDS probe, the darker contrast suggests that these areas should contain elements with a smaller atomic number than the average one, a condition which is fully satisfied by Ti. Moreover, their shape and distribution closely resembles those of similar $Ni_3(Ti,Al)$ precipitates, which were detected and described in several HEAs [18,47] as well as in Ni-based alloys [48] and marageing steels [23]. The recognition of Ni_3Ti precipitates is also made particularly difficult by the fact that the lattice constants of $L1_2$ Ni_3Ti (3.618 Å [49]) and that of the CoCuFeMnNi matrix (3.617 Å) coincide to a large extent: in fact, such coincidence makes it very hard to distinguish the two phases both by S-XRD and AC-STEM analyses. These precipitates would be usually expected to rapidly evolve into the thermodynamically stable HCP form, as predicted by CALPHAD simulation: in the present case, however, they appear to be rather stable, as no evident sign of overageing was found during ageing tests. The relative stability of the $L1_2$ crystalline form of Ni_3Ti precipitates might be attributed to the proposed mechanism of sluggish diffusion, which may characterize HEAs [50]. However, it has been previously demonstrated that the CoCuFeMnNi alloy does not display any such effect [30] and the retainment of the cubic structure may therefore be rather attributed to the fact that the coherency relation with the FCC matrix allows a large reduction in the precipitates' interfacial energy [51]. Finally, the recognition of the observed $L1_2$ nanometric clusters as Ni_3Ti phase is further supported by the results of calorimetric analyses (Section 4.1): the exothermic peak A' lies between 280 °C and 420 °C, a temperature range that is related to the precipitation of hardening intermetallic phases, including Ni_3Ti , in maraging steels [52,53]. Moreover, the endothermic peak C corresponds to the temperature range usually associated to the dissolution of hardening phases in the above mentioned steels.

5.2 Mechanical behaviour

The role played by each of the observed microstructural features in strengthening the studied alloys at ambient temperature was evaluated through the implementation of different models. The different contributions to the total yield strength are collected in Table 3 and Figure 8. Moreover, all the parameters considered for computation and their origins are reported in the supporting material section, in Tables S1, S2 and S3.

Yield strength of polycrystalline metallic materials is usually described as the sum of individual contributions:

$$\sigma_y = \sigma_{fr} + \sigma_{GB} + \sigma_{SH} + \sigma_{SS} + \sigma_{SP} \quad (1)$$

where σ_{fr} is the intrinsic lattice frictional stress, σ_{GB} is the grain boundary strengthening, σ_{SH} is the strain hardening caused by dislocations, σ_{SS} is the solid solution strengthening and σ_{SP} is the second-phase strengthening. σ_{fr} is considered constant in all the considered conditions (34 MPa); similarly, σ_{SH} is neglected, as no dislocation was observed during ac-STEM analyses.

Grain boundary strengthening

The contribution to strength given by grain boundaries is expressed by the well-known Hall-Petch relation:

$$\sigma_{GB} = Kd^{-\frac{1}{2}} \quad (2)$$

where K is the Hall-Petch constant and d is the grain size. Since the grain size was very limitedly affected by both the alloy composition and the applied thermal treatment, this contribution resulted to be fairly constant in all the considered conditions (46.8 MPa for CoCuFeMnNi alloy and 46.7 MPa for $CoCuFeMnNiTi_{0.13}$ alloy, regardless of the thermal treatment condition)

Solid solution strengthening

In the base alloy, σ_{SS} was computed by subtracting the contribution of other mechanisms from the total σ_y, as no straight-forward model for computing such contribution in HEAs exists [54,55]: as expected, results show that this contribution is more significative in solution-treated condition (56.5 MPa) than after ageing treatment (29.5 MPa). As far as the Ti-modified alloy is concerned, the contribution of the doping element to the alloy's strength may be evaluated through a common substitutional solid solution model, according to the following expression [56]:

$$\sigma_{SS(Ti)} = M\frac{G_{Ti}c^2\varepsilon_{Ti}^{\frac{3}{2}}}{700} \quad (3)$$

where M is the Taylor factor, G_{Ti} is the shear modulus of Ti, c is its concentration and ε_{Ti} is an interaction parameter describing the change of the alloy's lattice parameter a as a function of Ti concentration ($\varepsilon_{Ti} \approx \frac{1}{a}\frac{da}{dc}$). Computations show that the lattice strain caused by the presence of the larger Ti atoms results in strength contribution of about 31.6 MPa, which agrees well with available literature results [56]. Finally, it is worth highlighting that this contribution was assumed to be negligible after ageing treatment.

Second phase strengthening

The strengthening caused by second phases can be described in different ways, depending on the nature and the main characteristics of such phases. In particular, different models have to be applied in the current study, as phases supposedly resulting from both spinodal decomposition (Cu-rich clusters in solution treated samples and maze-like discs in peak-aged samples) and proper precipitation (Ni_3Ti precipitates in peak-aged Ti-containing alloy) were found.

Strengthening through spinodal decomposition has been addressed over the years by several works: the models, which have been proposed, are admirably collected and discussed in [57]. Among the available descriptions, those proposed by Kato appear to have drawn considerable appreciation and have been successfully applied to HEAs [58]. Two contributions to strength are considered in such models, namely the modulations of lattice strain and elastic modulus. In [59] Kato examined FCC spinodal alloys, characterized by a limited amplitude of compositional variations. He concluded that the elastic modulus modulation could be neglected because of the small variation of local composition, whereas the lattice strain modulation played a pivotal role. The resulting strengthening was demonstrated to be independent of the modulation's wavelength. Conversely, in [60] the same effect in BCC alloys was shown to stem from both contributions: the strain component was still found to be wavelength – independent, whereas the modulus contribution was not. As the large modulation of Cu content in the present alloys may lead to a substantial variation of elastic properties, both lattice strain (σ_L) and modulus (σ_M) contributions will be considered in the present work, according to the following equation:

$$\sigma_{SD} = \sigma_L + \sigma_M = \frac{A|\varepsilon|Y}{\sqrt{6}} + 0.65\frac{\Delta G\, b}{\lambda} \quad (4)$$

where A is the amplitude of the compositional modulation, ε is the lattice mismatch parameter describing the change of the local lattice parameter a as a function of composition ($\varepsilon \approx \frac{1}{a}\frac{da}{dc}$), Y depends on the elastic constants C_{ij} and for {100} modulations can be computed as $Y = \frac{(C_{11}-C_{12})(C_{11}+2C_{12})}{C_{11}}$, ΔG is the difference in shear moduli induced by compositional fluctuations , b is Burger's vector and λ is the wavelength of the modulation. The rounded clusters detected in solution treated samples are characterized by an evident Cu enrichment but by no change in lattice parameter with respect to the matrix; on the contrary, in the peak-aged condition the discs composing the maze-like structure display differences in both composition and lattice parameter. Therefore, the second term only (σ_M) shall be considered in solution treated condition, whereas both mechanisms (σ_L and σ_M) are activated by ageing treatment. Computations show that the two alloys are strengthened to similar extents by the phases resulting from spinodal decomposition processes. In particular, a somehow greater effect is caused in the Ti-modified alloy by the slightly larger amplitude of compositional modulation and by the partial segregation of Ti inside Cu-rich clusters / discs, which is connected to an increased variation of local modulus and lattice parameter. Finally, it shall be underlined that, if models usually applied to precipitation strengthening were to be applied to the present phases,

strength values largely exceeding the experimental ones would be found. This point may represent a further hint supporting the claim that the origin of the Cu-rich second phases lies in a spinodal decomposition process.

As far as precipitation hardening is concerned, several models have been proposed, too. In particular, a dislocation by-pass mechanism (Orowan strengthening) is predominant if precipitates are relatively large and incoherent with respect to the matrix; whereas lattice distortion and chemical hardening effects shall be considered if precipitates are small and coherent. The strength contribution provided by Orowan by-pass mechanism is given by the following equation:

$$\sigma_{OR} = M \frac{0.4Gb}{\pi\sqrt{1-\nu}} \frac{\ln\left(\frac{d}{b}\right)}{\lambda} \quad (5)$$

Where d is the average precipitate diameter and λ is the interparticle spacing. The dependence on d shown by Equation 5, as well as available literature data [27], indicate that this mechanism becomes relevant only if the diameter of precipitates exceeds 200 nm. In this light, and considering the microstructure shown by the $CoCuFeMnNiTi_{0.13}$ alloy, it may be safely assumed that Orowan strengthening may be neglected. Ni_3Ti precipitates are both extremely fine and fully coherent to the matrix: therefore, contributions from coherency (σ_C), modulus mismatch (σ_{MM}) and order strengthening (σ_O) shall be considered, depending on dislocations actually shearing precipitates or not [61]. The former two effects contribute to strength before shearing, whereas the latter one acts during shearing: as a consequence, the larger between $\sigma_C + \sigma_{MM}$ and σ_O shall be considered as the overall strength contribution provided by coherent precipitates. Such contributions can be computed by the following equations:

$$\sigma_C = M\alpha_\varepsilon (G\varepsilon_c)^{\frac{3}{2}} \left(\frac{df}{Gb}\right)^{\frac{1}{2}} \quad (6)$$

$$\sigma_{MM} = M\ 0.0055(\Delta G)^{\frac{3}{2}} \left(\frac{2f}{G}\right)^{\frac{1}{2}} \left(\frac{d}{2b}\right)^{\frac{3m}{2}-1} \quad (7)$$

$$\sigma_O = M\ 0.81\ \frac{\gamma_{apb}}{2b} \left(\frac{3\pi f}{8}\right)^{\frac{1}{2}} \quad (8)$$

Where α_ε is 2.6 for FCC metals; $\varepsilon_c \approx \frac{2}{3}\frac{\Delta a}{a}$ is the constrained lattice parameter, with Δα being the difference in lattice parameter between the Ni_3Ti precipitate and the FCC matrix; d and f are the precipitate's diameter and volume fraction, respectively; ΔG is the difference in shear moduli between the matrix and the precipitate; m = 0.85; γ_{apb} is the anti-phase boundary energy of the precipitates. The computed values, which are reported in Table 3, suggest that Ni_3Ti precipitates mainly strengthen the alloy before being sheared by dislocation, since $\sigma_O < \sigma_C + \sigma_{MM}$. Moreover, the contribution of σ_C (1.3 MPa) is negligible with respect to σ_{MM} (133.8 MPa): such result stems from the almost zero difference in lattice parameter between the

precipitate and the matrix and, conversely, from the relevant change in elastic modulus between the two phases. The present computation may overestimate the strength contribution of Ni_3Ti precipitates: in fact the equilibrium volume fraction for such phase, derived from CALPHAD simulation, was used. The actual amount of formed precipitates is likely lower, but the use of the equilibrium fraction may still represent a sensible assumption. Indeed, hardness curves collected on prolonged ageing at 630 °C (up to 4 days, Figure S2) show a very stable plateau from 6 h onwards.

The results of the reported computations are summed and visually collected in Figure 8. Since the generic solid solution strengthening is computed as the difference between experimental strength values and the sum of all other contributions, the computed overall strength values obviously fit the experimental ones for the CoCuFeMnNi alloy. On the other hand, it is remarkable that an extremely good agreement is found between theoretical and experimental values in the case of the $CoCuFeMnNiTi_{0.13}$ alloy, too. The present analysis shows that the dominant strengthening contribution is given by the spinodal decomposition, modulus-related strengthening in solution-treated alloys. After ageing treatment, the lattice strain induced by Cu-rich discs becomes the main contribution in both alloys but is effectively backed by the modulus mismatch strengthening related to the formation of Ni_3Ti precipitates. Indeed, such results confirm that the observed second phases mainly influence dislocation motion at long range through the continuous modulation of local lattice strain and elastic properties, rather than by being properly sheared [62].

Table 3. Theoretical contributions of the discussed strengthening mechanisms in CoCuFeMnNi and $CoCuFeMnNiTi_{0.13}$ alloys in solution-treated and peak-aged conditions.

Mechanism (MPa)		CoCuFeMnNi		$CoCuFeMnNiTi_{0.13}$	
		Solution-treated	Peak-aged	Solution-treated	Peak-aged
Frictional stress		**34.0**	**34.0**	**34.0**	**34.0**
Hall-Petch strengthening		**46.8**	**46.8**	**46.7**	**46.7**
Solid solution strengthening		**56.5**	**29.5**	**56.5**	**29.5**
Solid solution strengthening- Ti		-	-	**31.6**	**0**
Spinodal strengthening	Lattice strain contribution	**0**	**248.6**	**0**	**290.2**
	Modulus contribution	**70.3**	**39.7**	**112.8**	**50.9**
Precipitation strengthening	Coherency strengthening	**-**	**-**	**-**	**1.3**
	Modulus mismatch strengthening	**-**	**-**	**-**	**133.8**
	Order strengthening	**-**	**-**	**-**	**19.8**

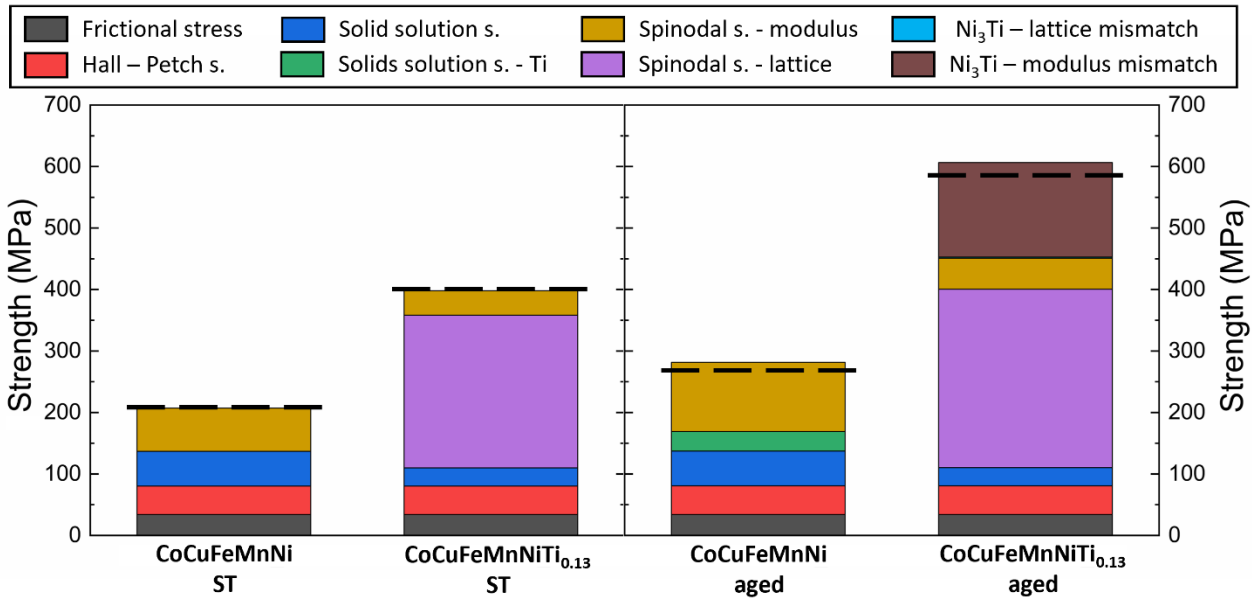

Figure 8. Theoretical contributions of the discussed strengthening mechanisms in CoCuFeMnNi and $CoCuFeMnNiTi_{0.13}$ alloys in solution-treated and peak-aged conditions. Black dotted lines represent the experimentally measured yield strength values.

Plastic deformation behaviour

The trend of stress – strain curves recorded for all the considered conditions at both ambient and cryogenic temperatures suggests that, at first glance, no difference exists in the deformation behaviour between CoCuFeMnNi and $CoCuFeMnNiTi_{0.13}$ alloys. Indeed, previous works demonstrated that plastic deformation in the lean alloy is dominated by dislocation slip, regardless of the testing temperature, and that no twinning or transformation-based mechanism is present [15,63]. It might be expected that the presence of Ni_3Ti could raise the threshold stress for dislocation slip and thus enable the activation of other deformation mechanisms. Nevertheless, the present results provide no hint of such a shift. In this respect, it shall be observed that Cu is known to strongly increase the stacking fault energy in both conventional [64] and high entropy alloys [65]; moreover, Cu was also shown to retard the kinetics of twin formation [66]. It is therefore likely that the stress needed for the activation of twinning in the present alloy is still much higher than the one required by dislocation slip and is not sufficiently affected by the presence of Ni_3Ti precipitates.

6. Summary and conclusions

A novel high entropy alloy was mechanistically designed to be strengthened by concurrent precipitation and spinodal hardening. An equiatomic CoCuFeMnNi alloy was modified through the addition of Ti and a target composition ($CoCuFeMnNiTi_{0.13}$) was selected by means of CALPHAD simulation.

The compositional modification allowed to obtain an alloy, which, after a proper thermal treatment schedule, is synergistically strengthened by phases resulting from two different mechanisms. Since spinodal decomposition and precipitation of Ni_3Ti concern different atomic species (Cu – Fe – Co and Ni – Ti, respectively) and rely on different mechanisms (short range diffusion vs. nucleation and growth based on long range diffusion), the two mechanisms do not interfere with each other and the resulting effects can be safely superimposed. Coherent, Cu-rich discs arranged in a nano-scale maze-like structure are produced by the spinodal decomposition of the supersaturated matrix and strengthen the alloy through the periodic modulation of local lattice strain and elastic properties. Conversely, coherent, extremely fine Ni_3Ti phases with $L1_2$ ordered structure arise from a proper precipitation process and mainly strengthen the alloy thanks to the mismatch between their modulus and the one of the surrounding matrix. This combination of different mechanisms allowed to obtain an improvement of almost 200 MPa in the alloy's yield strength after ageing treatment, while at the same time retaining a remarkable ductility (17.7 %).

In summary, the behaviour and possibilities of the $CoCuFeMnNiTi_{0.13}$ HEA are determined by the simultaneous presence of Cu and Ti, which are able to induce the formation of coherent-only phases through two distinct and concurrent formation mechanisms, i.e. spinodal decomposition of Cu-rich phases and proper precipitation of Ni_3Ti.

Acknowledgements

The authors would like to acknowledge Marco Pini, Nicola Bennato and Enrico Bassani from CNR ICMATE, Paolo Pecoraro, Luca Signorelli, Lorenzo Giudici, Ludovica Rovatti and Rasheed Michael Ishola from Politecnico di Milano and Catherine Dejoie form ESRF for their assistance in the experiments. Access to the David Cockayne Centre for Electron Microscopy (DCCEM) facilities of the University of Oxford was funded by the European Union's Horizon 2020 research and innovation programme under grant agreement No 823717 – ESTEEM3 (project ATHEnA). We acknowledge the ESRF for provision of beam time.

Data availability statement

The raw/processed data required to reproduce these findings cannot be shared at this time as the data also forms part of an ongoing study.

References

[1] B. Cantor, I.T.H. Chang, P. Knight, A.J.B. Vincent, Microstructural development in equiatomic multicomponent alloys, Mater. Sci. Eng. A. 375–377 (2004) 213–218. https://doi.org/10.1016/j.msea.2003.10.257.

[2] J.W. Yeh, S.K. Chen, S.J. Lin, J.Y. Gan, T.S. Chin, T.T. Shun, C.H. Tsau, S.Y. Chang, Nanostructured high-entropy alloys with multiple principal elements: Novel alloy design concepts and outcomes, Adv. Eng. Mater. 6 (2004) 299–303. https://doi.org/10.1002/adem.200300567.

[3] E.P. George, D. Raabe, R.O. Ritchie, High-entropy alloys, Nat. Rev. Mater. 4 (2019) 515–534. https://doi.org/10.1038/s41578-019-0121-4.

[4] X. Gao, Y. Lu, J. Liu, J. Wang, T. Wang, Y. Zhao, Extraordinary ductility and strain hardening of Cr26Mn20Fe20Co20Ni14 TWIP high-entropy alloy by cooperative planar slipping and twinning, Materialia. 8 (2019) 100485. https://doi.org/10.1016/j.mtla.2019.100485.

[5] P.K. Shurkin, N. V. Letyagin, A.I. Yakushkova, M.E. Samoshina, D.Y. Ozherelkov, T.K. Akopyan, Remarkable thermal stability of the Al-Ca-Ni-Mn alloy manufactured by laser-powder bed fusion, Mater. Lett. (2020) 129074. https://doi.org/10.1016/j.matlet.2020.129074.

[6] Z. Li, S. Zhao, R.O. Ritchie, M.A. Meyers, Mechanical properties of high-entropy alloys with emphasis on face-centered cubic alloys, Prog. Mater. Sci. 102 (2019) 296–345. https://doi.org/10.1016/j.pmatsci.2018.12.003.

[7] C.C. Koch, Nanocrystalline high-entropy alloys, J. Mater. Res. 32 (2017) 3435–3444. https://doi.org/10.1557/jmr.2017.341.

[8] S.S. Nene, M. Frank, K. Liu, R.S. Mishra, B.A. McWilliams, K.C. Cho, Extremely high strength and work hardening ability in a metastable high entropy alloy, Sci. Rep. 8 (2018) 1–8. https://doi.org/10.1038/s41598-018-28383-0.

[9] L. Liu, Y. Zhang, J. Han, X. Wang, W. Jiang, C.-T. Liu, Z. Zhang, P. Liaw, Nanoprecipitate-Strengthened High-Entropy Alloys, Adv. Sci. 8 (2021) 1–20.

[10] H. Luan, L. Huang, B. Luo, X. Yang, J. Li, Z. Han, J. Si, Y. Shao, K.-F. Yao, Spinodal Decomposition and the Pseudo-Binary Decomposition in High-Entropy Alloys, SSRN Electron. J. 248 (2022) 118775. https://doi.org/10.2139/ssrn.4104199.

[11] L. Li, Z. Li, A. Kwiatkowski da Silva, Z. Peng, H. Zhao, B. Gault, D. Raabe, Segregation-driven grain boundary spinodal decomposition as a pathway for phase nucleation in a high-entropy alloy, Acta Mater. 178 (2019) 1–9. https://doi.org/10.1016/j.actamat.2019.07.052.

[12] H. Li, Y. Han, H. Feng, G. Zhou, Z. Jiang, M. Cai, Y. Li, M. Huang, Enhanced strength-ductility synergy via high dislocation density-induced strain hardening in nitrogen interstitial CrMnFeCoNi high-entropy alloy, J. Mater. Sci. Technol. 141 (2023) 184–192. https://doi.org/10.1016/j.jmst.2022.09.020.

[13] Z. Wang, I. Baker, Z. Cai, S. Chen, J.D. Poplawsky, W. Guo, The effect of interstitial carbon on the mechanical properties and dislocation substructure evolution in Fe40.4Ni11.3Mn34.8Al7.5Cr6 high entropy alloys, Acta Mater. 120 (2016) 228–239. https://doi.org/10.1016/j.actamat.2016.08.072.

[14] S. Gorsse, J.P. Couzinié, D.B. Miracle, From high-entropy alloys to complex concentrated alloys, Comptes Rendus Phys. 19 (2018) 721–736. https://doi.org/10.1016/j.crhy.2018.09.004.

[15] J. Fiocchi, A. Mostaed, M. Coduri, A. Tuissi, R. Casati, Enhanced cryogenic and ambient temperature mechanical properties of CoCuFeMnNi high entropy alloy through controlled heat treatment, J. Alloys Compd. 910 (2022) 164810. https://doi.org/10.1016/j.jallcom.2022.164810.

[16] S. Mohanty, N.P. Gurao, P. Padaikathan, K. Biswas, Ageing behaviour of equiatomic consolidated Al20Co20Cu20Ni20Zn20 high entropy alloy, Mater. Charact. 129 (2017) 127–134. https://doi.org/10.1016/j.matchar.2017.04.011.

[17] K. Ming, X. Bi, J. Wang, Precipitation strengthening of ductile Cr15Fe20Co35Ni20Mo10 alloys, Scr. Mater. 137 (2017) 88–93. https://doi.org/10.1016/j.scriptamat.2017.05.019.

[18] Y. Tong, D. Chen, B. Han, J. Wang, R. Feng, T. Yang, C. Zhao, Y.L. Zhao, W. Guo, Y. Shimizu, C.T. Liu, P.K. Liaw, K. Inoue, Y. Nagai, A. Hu, J.J. Kai, Outstanding tensile properties of a precipitation-strengthened FeCoNiCrTi0.2 high-entropy alloy at room and cryogenic temperatures, Acta Mater. 165 (2019) 228–240. https://doi.org/10.1016/j.actamat.2018.11.049.

[19] K. Hagihara, T. Nakano, Y. Umakoshi, Plastic deformation behaviour in Ni3Ti single crystals with D024 structure, Acta Mater. 51 (2003) 2623–2637. https://doi.org/10.1016/S1359-6454(03)00060-0.

[20] H. Long, S. Mao, Y. Liu, Z. Zhang, X. Han, Microstructural and compositional design of Ni-based single crystalline superalloys d A review, J. Alloys Compd. 743 (2018) 203–220. https://doi.org/10.1016/j.jallcom.2018.01.224.

[21] W. Sha, H. Leitner, Z. Guo, W. Xu, Phase transformations in maraging steels, Phase Transform.

588 Steels. (2012) 332–362. https://doi.org/10.1533/9780857096111.2.332.

589 [22] M. Niu, G. Zhou, W. Wang, M.B. Shahzad, Y. Shan, Precipitate evolution and strengthening behavior
590 during aging process in a 2.5 GPa grade maraging steel, Acta Mater. 179 (2019) 296–307.
591 https://doi.org/10.1016/j.actamat.2019.08.042.

592 [23] D.M. Vanderwalker, The Precipitation Sequence of Ni3Ti in Co-Free Maraging Steel, Metall. Trans. A.
593 18 (1987) 1191–1194.

594 [24] B. Han, J. Wei, Y. Tong, D. Chen, Y. Zhao, J. Wang, F. He, T. Yang, C. Zhao, Y. Shimizu, K. Inoue, Y.
595 Nagai, A. Hu, C.T. Liu, J.J. Kai, Composition evolution of gamma prime nanoparticles in the Ti-doped
596 CoFeCrNi high entropy alloy, Scr. Mater. 148 (2018) 42–46.
597 https://doi.org/10.1016/j.scriptamat.2018.01.025.

598 [25] Y. Chen, H.W. Deng, Z.M. Xie, M.M. Wang, J.F. Yang, T. Zhang, Y. Xiong, R. Liu, X.P. Wang, Q.F. Fang,
599 C.S. Liu, Tailoring microstructures and tensile properties of a precipitation-strengthened
600 (FeCoNi)94Ti6 medium-entropy alloy, J. Alloys Compd. 828 (2020) 154457.
601 https://doi.org/10.1016/j.jallcom.2020.154457.

602 [26] T. Yang, Y.L. Zhao, Y. Tong, Z.B. Jiao, J. Wei, J.X. Cai, X.D. Han, D. Chen, A. Hu, J.J. Kai, K. Lu, Y. Liu, C.T.
603 Liu, Multicomponent intermetallic nanoparticles and superb mechanical behaviors of complex
604 alloys, Science (80-.). 362 (2018) 933–937. https://doi.org/10.1126/science.aas8815.

605 [27] Y.Y. Zhao, H.W. Chen, Z.P. Lu, T.G. Nieh, Thermal stability and coarsening of coherent particles in a
606 precipitation-hardened (NiCoFeCr)94Ti2Al4 high-entropy alloy, Acta Mater. 147 (2018) 184–194.
607 https://doi.org/10.1016/j.actamat.2018.01.049.

608 [28] B.E. MacDonald, Z. Fu, X. Wang, Z. Li, W. Chen, Y. Zhou, D. Raabe, J. Schoenung, H. Hahn, E.J.
609 Lavernia, Influence of phase decomposition on mechanical behavior of an equiatomic CoCuFeMnNi
610 high entropy alloy, Acta Mater. 181 (2019) 25–35. https://doi.org/10.1016/j.actamat.2019.09.030.

611 [29] C. Dejoie, M. Coduri, S. Petitdemange, C. Giacobbe, E. Covacci, O. Grimaldi, P.O. Autran, M.W.
612 Mogodi, D.Š. Jung, A.N. Fitch, Combining a nine-crystal multi-analyser stage with a two-dimensional
613 detector for high-resolution powder X-ray diffraction, J. Appl. Crystallogr. 51 (2018) 1721–1733.
614 https://doi.org/10.1107/S1600576718014589.

615 [30] R. Sonkusare, P. Divya Janani, N.P. Gurao, S. Sarkar, S. Sen, K.G. Pradeep, K. Biswas, Phase equilibria
616 in equiatomic CoCuFeMnNi high entropy alloy, Mater. Chem. Phys. 210 (2018) 269–278.
617 https://doi.org/10.1016/j.matchemphys.2017.08.051.

[31] Y.U. Heo, H.C. Lee, The twin and twin system in FCT L10 θ-MnNi phase in an equiatomic Mn-Ni alloy, Mater. Trans. 48 (2007) 2546–2550. https://doi.org/10.2320/matertrans.MD200782.

[32] C.M. Lin, H.L. Tsai, Equilibrium phase of high-entropy FeCoNiCrCu0.5 alloy at elevated temperature, J. Alloys Compd. 489 (2010) 30–35. https://doi.org/10.1016/j.jallcom.2009.09.041.

[33] A. Taylor, X-ray Metallography, Wiley, New York, 1961.

[34] H.M. Tawancy, On the Role of Superlattice Structures with Ni3X-type Composition in Selected Ni-Based Superalloys with Commercial Grades, Metallogr. Microstruct. Anal. 8 (2019) 591–606. https://doi.org/10.1007/s13632-019-00571-y.

[35] Y. Liang, L. Wang, Y. Wen, B. Cheng, Q. Wu, T. Cao, Q. Xiao, Y. Xue, G. Sha, Y. Wang, Y. Ren, X. Li, L. Wang, F. Wang, H. Cai, High-content ductile coherent nanoprecipitates achieve ultrastrong high-entropy alloys, Nat. Commun. (n.d.) 1–8. https://doi.org/10.1038/s41467-018-06600-8.

[36] H. Chen, X. Yuan, W. Ren, J. Peng, B. Ding, T. Zheng, J. Yu, P.K. Liaw, Y. Zhong, A new single crystal high entropy alloy with excellent high-temperature tensile property, Mater. Res. Express. 7 (2020). https://doi.org/10.1088/2053-1591/ab8491.

[37] M. Scavini, M. Coduri, M. Allieta, P. Masala, S. Cappelli, C. Oliva, M. Brunelli, F. Orsini, C. Ferrero, Percolating hierarchical defect structures drive phase transformation in Ce1-xGdxO2-x/2: A total scattering study, IUCrJ. 2 (2015) 511–522. https://doi.org/10.1107/S2052252515011641.

[38] P. Scardi, M. Leoni, Diffraction whole-pattern modelling study of anti-phase domains in Cu 3Au, Acta Mater. 53 (2005) 5229–5239. https://doi.org/10.1016/j.actamat.2005.08.002.

[39] M. Palumbo, S. Curiotto, L. Battezzati, Thermodynamic analysis of the stable and metastable Co-Cu and Co-Cu-Fe phase diagrams, Calphad Comput. Coupling Phase Diagrams Thermochem. 30 (2006) 171–178. https://doi.org/10.1016/j.calphad.2005.10.007.

[40] R.P. Shi, C.P. Wang, D. Wheeler, X.J. Liu, Y. Wang, Formation mechanisms of self-organized core/shell and core/shell/corona microstructures in liquid droplets of immiscible alloys, Acta Mater. 61 (2013) 1229–1243. https://doi.org/10.1016/j.actamat.2012.10.033.

[41] M. Tang, A. Karma, Surface modes of coherent spinodal decomposition, Phys. Rev. Lett. 108 (2012) 1–5. https://doi.org/10.1103/PhysRevLett.108.265701.

[42] Y. Zhang, Z. Chen, D. Cao, J. Zhang, P. Zhang, Q. Tao, X. Yang, Concurrence of spinodal decomposition and nano-phase precipitation in a multi-component AlCoCrCuFeNi high-entropy alloy, J. Mater. Res. Technol. 8 (2019) 726–736. https://doi.org/10.1016/j.jmrt.2018.04.020.

[43] M.A. Turchanin, P.G. Agraval, I. V. Nikolaenko, Thermodynamics of alloys and phase equilibria in the copper-iron system, J. Phase Equilibria. 24 (2003) 307–319. https://doi.org/10.1361/105497103770330280.

[44] J.Z. Jiang, C. Gente, R. Bormann, Mechanical alloying in the Fe-Cu system, Mater. Sci. Eng. A. 242 (1998) 268–277. https://doi.org/10.1016/s0921-5093(97)00522-4.

[45] C.M. Lin, H.L. Tsai, Effect of annealing treatment on microstructure and properties of high-entropy FeCoNiCrCu0.5 alloy, Mater. Chem. Phys. 128 (2011) 50–56. https://doi.org/10.1016/j.matchemphys.2011.02.022.

[46] S. Sheibani, S. Heshmati-Manesh, A. Ataie, A. Caballero, J.M. Criado, Spinodal decomposition and precipitation in Cu-Cr nanocomposite, J. Alloys Compd. 587 (2014) 670–676. https://doi.org/10.1016/j.jallcom.2013.11.019.

[47] Z. Fu, L. Jiang, J.L. Wardini, B.E. Macdonald, H. Wen, W. Xiong, D. Zhang, Y. Zhou, T.J. Rupert, W. Chen, E.J. Lavernia, A high-entropy alloy with hierarchical nanoprecipitates and ultrahigh strength, (2018) 1–9.

[48] S. Asgari, Age-Hardening Behavior and Phase Identification in Solution-Treated AEREX 350 Superalloy, Metall. Mater. Trans. A. 37 (2006) 2006–2051.

[49] Y. Cao, J. Zhu, Y. Liu, Z. Lai, Z. Nong, First-principles studies of the structural, elastic, electronic and thermal properties of γ′-Ni3Ti, Phys. B Condens. Matter. 412 (2013) 45–49. https://doi.org/10.1016/j.physb.2012.12.020.

[50] M.H. Tsai, J.W. Yeh, High-entropy alloys: A critical review, Mater. Res. Lett. 2 (2014) 107–123. https://doi.org/10.1080/21663831.2014.912690.

[51] Y.Y. Zhao, H.W. Chen, Z.P. Lu, T.G. Nieh, Acta Materialia Thermal stability and coarsening of coherent particles in a precipitation-hardened (NiCoFeCr) 94 Ti 2 Al 4 high-entropy alloy, 147 (2018) 184–194. https://doi.org/10.1016/j.actamat.2018.01.049.

[52] C.M.I.L.A. Molinari, Phase transformation in a nanostructured M300 maraging steel obtained by SPS of mechanically alloyed powders, J. Therm. Anal. Calorim. 101 (2010) 815–821. https://doi.org/10.1007/s10973-010-0745-5.

[53] Z. Guo, W. Sha, D. Li, Quantification of phase transformation kinetics of 18 wt .% Ni C250 maraging steel, Mater. Sci. Eng. A. 373 (2004) 10–20. https://doi.org/10.1016/j.msea.2004.01.040.

[54] I. Toda-Caraballo, A general formulation for solid solution hardening effect in multicomponent

alloys, Scr. Mater. 127 (2017) 113–117. https://doi.org/10.1016/j.scriptamat.2016.09.009.

[55] H.W. Yao, J.W. Qiao, J.A. Hawk, H.F. Zhou, M.W. Chen, M.C. Gao, Mechanical properties of refractory high-entropy alloys: Experiments and modeling, J. Alloys Compd. 696 (2017) 1139–1150. https://doi.org/10.1016/j.jallcom.2016.11.188.

[56] H. Shahmir, M. Nili-Ahmadabadi, A. Shafiee, M. Andrzejczuk, M. Lewandowska, T.G. Langdon, Effect of Ti on phase stability and strengthening mechanisms of a nanocrystalline CoCrFeMnNi high-entropy alloy, Mater. Sci. Eng. A. 725 (2018) 196–206. https://doi.org/10.1016/j.msea.2018.04.014.

[57] I. Baker, R.K. Zheng, D.W. Saxey, S. Kuwano, M.W. Wittmann, J.A. Loudis, K.S. Prasad, Z. Liu, R. Marceau, P.R. Munroe, S.P. Ringer, Microstructural evolution of spinodally formed Fe35Ni15Mn25Al25, Intermetallics. 17 (2009) 886–893. https://doi.org/10.1016/j.intermet.2009.03.016.

[58] I. Basu, J.T.M. De Hosson, Strengthening mechanisms in high entropy alloys: Fundamental issues, Scr. Mater. 187 (2020) 148–156. https://doi.org/10.1016/j.scriptamat.2020.06.019.

[59] M. Kato, T. Mori, L.H. Schwartz, Hardening by spinodal Modulated structure, Acta Metall. 28 (1980) 285–290.

[60] M. Kato, Harding by soinodal modulated structure in b.c.c. alloys, Acta Metall. 29 (1981) 79–87.

[61] J.Y. He, H. Wang, H.L. Huang, X.D. Xu, M.W. Chen, Y. Wu, X.J. Liu, T.G. Nieh, K. An, Z.P. Lu, A precipitation-hardened high-entropy alloy with outstanding tensile properties, Acta Mater. 102 (2016) 187–196. https://doi.org/10.1016/j.actamat.2015.08.076.

[62] R. Agarwal, R. Sonkusare, S.R. Jha, N.P. Gurao, K. Biswas, N. Nayan, Understanding the deformation behavior of CoCuFeMnNi high entropy alloy by investigating mechanical properties of binary ternary and quaternary alloy subsets, Mater. Des. 157 (2018) 539–550. https://doi.org/10.1016/j.matdes.2018.07.046.

[63] Tazuddin, K. Biswas, N.P. Gurao, Deciphering micro-mechanisms of plastic deformation in a novel single phase fcc-based MnFeCoNiCu high entropy alloy using crystallographic texture, Mater. Sci. Eng. A. 657 (2016) 224–233. https://doi.org/10.1016/j.msea.2016.01.065.

[64] B.C. De Cooman, Y. Estrin, S.K. Kim, Twinning-induced plasticity (TWIP) steels, Acta Mater. 142 (2018) 283–362. https://doi.org/10.1016/j.actamat.2017.06.046.

[65] S.H. Shim, S.M. Oh, J. Lee, S.K. Hong, S.I. Hong, Nanoscale modulated structures by balanced distribution of atoms and mechanical/structural stabilities in CoCuFeMnNi high entropy alloys,

Mater. Sci. Eng. A. 762 (2019) 138120. https://doi.org/10.1016/j.msea.2019.138120.

[66] J.K. Hwang, Effect of copper and aluminum contents on wire drawing behavior in twinning-induced plasticity steels, Mater. Sci. Eng. A. 737 (2018) 188–197. https://doi.org/10.1016/j.msea.2018.09.049.

[67] R. Sonkusare, K. Biswas, N. Al-Hamdany, H.G. Brokmeier, R. Kalsar, N. Schell, N.P. Gurao, A critical evaluation of microstructure-texture-mechanical behavior heterogeneity in high pressure torsion processed CoCuFeMnNi high entropy alloy, Mater. Sci. Eng. A. 782 (2020) 139187. https://doi.org/10.1016/j.msea.2020.139187.

[68] R.W. Cahan, P. Haasen, Physical Metallurgy, Elsevier B.V., Amsterdam, 1996.

[69] F. Tian, L.K. Varga, J. Shen, L. Vitos, Calculating elastic constants in high-entropy alloys using the coherent potential approximation: Current issues and errors, Comput. Mater. Sci. 111 (2016) 350–358. https://doi.org/10.1016/j.commatsci.2015.09.058.

[70] Z.G. Wang, W. Zhou, L.M. Fu, J.F. Wang, R.C. Luo, X.C. Han, B. Chen, X.D. Wang, Effect of coherent L12 nanoprecipitates on the tensile behavior of a fcc-based high-entropy alloy, Mater. Sci. Eng. A. 696 (2017) 503–510. https://doi.org/10.1016/j.msea.2017.04.111.

[71] M. Chandran, S.K. Sondhi, First-principle calculation of APB energy in Ni-based binary and ternary alloys, Model. Simul. Mater. Sci. Eng. 19 (2011). https://doi.org/10.1088/0965-0393/19/2/025008.

Supporting material

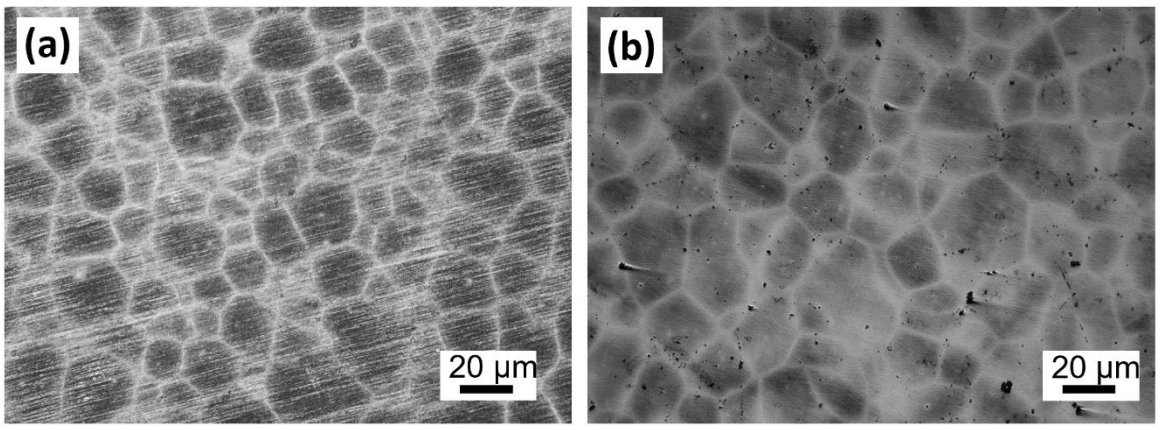

Figure S1: optical micrographs showing the grain structure of CoCuFeMnNi and $CoCuFeMnNiTi_{0.13}$ alloys, peak-aged at 630 °C.

730

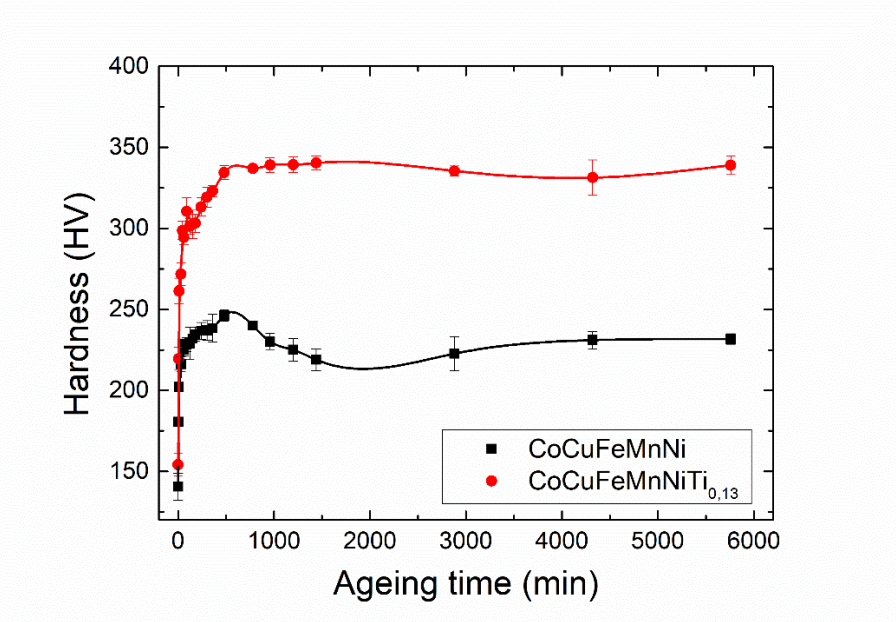

731

732 Figure S2: Ageing curves of CoCuFeMnNi and $CoCuFeMnNiTi_{0.13}$ alloys collected on isothermal holding at 630

733 °C for 4 days.

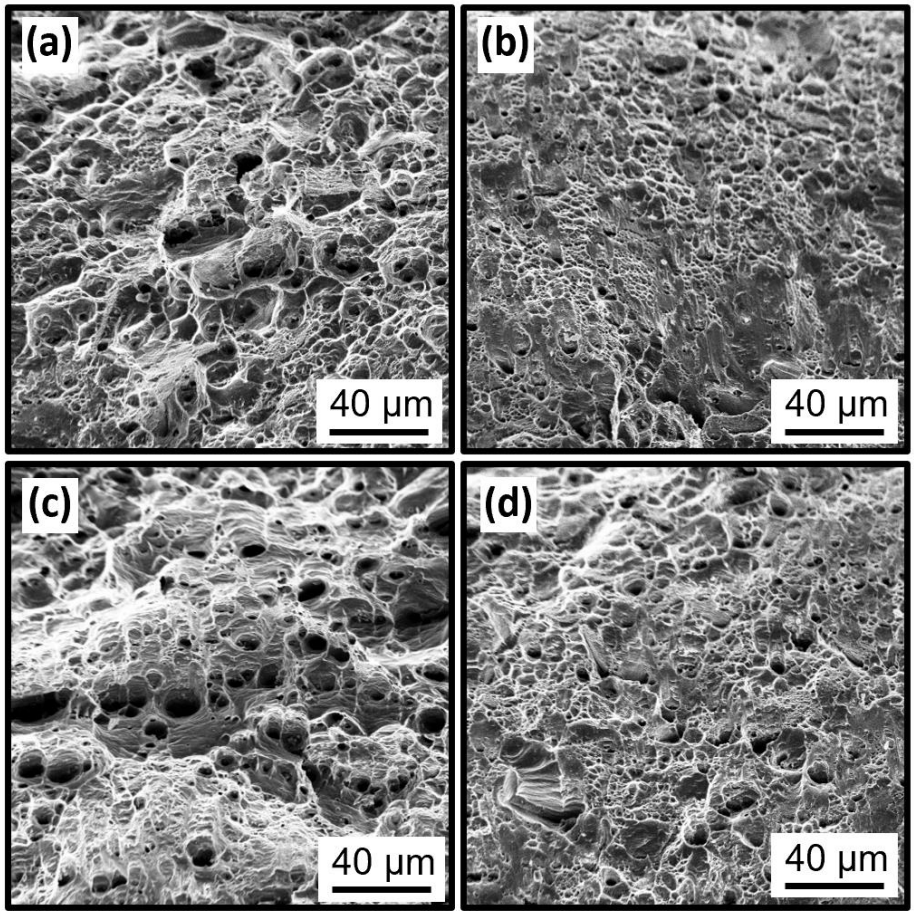

734

Figure S3: SEM micrographs depicting the fracture surfaces obtained after tensile tests at room temperature on CoCuFeMnNi alloy in solution-treated (a) and peak-aged (b) conditions and $CoCuFeMnNiTi_{0.13}$ alloy in solution-treated (c) and peak-aged (d) conditions.

Table S1. Strength contributions resulting from frictional stress, grain size and solid solution strengthening and related parameters. Experimental parameters were extracted from S-XRD and ac-STEM / EDS analyses.

Mechanism	Parameters	CoCuFeMnNi		$CoCuFeMnNiTi_{0.13}$		Source
		Solution-treated	Peak-aged	Solution-treated	Peak-aged	
Frictional stress	**Value (MPa)**	**34**	**34**	**34**	**34**	[67]
Hall-Petch strengthening	K	0.21	0.21	0,21	0,21	[67]
	d (µm)	20.1	20.1	20.2	20.2	Exp.
	Value (MPa)	**46.8**	**46.8**	**46.7**	**46.7**	
Solid solution strengthening	**Value (MPa)**	**56.5**	**29.5**	**56.5**	**29.5**	
Solid solution strengthening-Ti	M	-	-	3.06	-	[68]
	G_{Ti} (GPa)	-	-	44	-	[56]
	c (%)	-	-	2.5	-	Exp.
	ε_S	-	-	0.0884	-	$=\frac{\partial \ln(a)}{\partial c}$
	Value (MPa)	-	-	**31.6**	**0**	

Table S2. Strength contributions of the spinodal structure from different mechanisms and related parameters. Experimental parameters were extracted from S-XRD and ac-STEM / EDS analyses.

Mechanism	Parameters	CoCuFeMnNi		$CoCuFeMnNiTi_{0.13}$		Source
		Solution-treated	Peak-aged	Solution-treated	Peak-aged	
Lattice strain contribution	A	-	0.23	-	0.34	Exp.
	η	-	0.016	-	0.013	Exp.
	Y	162.6	162.6	162.6	162.6	$Y_{(100)}$ [69]
	Value (MPa)	**0**	**248.6**	**0**	**290.2**	
Modulus contribution	ΔG (GPa)	7.28	7.17	10.97	9.49	[68]
	b (nm)	0.26	0.26	0.26	0.26	Exp.
	λ (nm)	17.3	30	16.2	31	Exp.
	Value (MPa)	**70.3**	**39.7**	**112.8**	**50.9**	

Table S3. Strength contributions of the Ni_3Ti phase from different mechanisms and related parameters. Experimental parameters were extracted from S-XRD and ac-STEM / EDS analyses.

	CoCuFeMnNiTi$_{0.13}$ – peak-aged		
Mechanism	Parameters		Source
Coherency strengthening	M	3.06	[68]
	α_{ε}	2.6	[68]
	G (GPa)	73.75	Exp.
	ε_C	1.84x10^{-4}	$\approx \frac{2}{3}\frac{\Delta a}{a}$
	d (nm)	3	Exp.
	f	0.07	CALPHAD
	b (nm)	0.26	Exp.
	Value (MPa)	**1.3**	
Modulus mismatch strengthening	M	3,06	[68]
	ΔG (GPa)	23.25	Exp.
	f	0.07	CALPHAD
	G (GPa)	73.75	Exp.
	d (nm)	3	Exp.
	b (nm)	0.26	Exp.
	m	0,85	[70]
	Value (MPa)	**133.8**	
Order strengthening	M	3,06	[68]
	γ_{apb}	0.6	[71]
	b	0.26	Exp.
	f	0.07	CALPHAD
	Value (MPa)	**19.8**	